TU Delft

Delft University of Technology

Document Version
Final published version

Licence
CC BY

Citation (APA)
Trivedi, R., Sharma, S., Trivedi, V., Sharma, R., Groves, R. M., Sheoran, G., & Anand, A. (2026). Emissivity-independent spatiotemporal thermal anomaly detection in metal components using transmission-mode phase measuring deflectometry. *Optics and Laser Technology*, *203*, Article 115664. https://doi.org/10.1016/j.optlastec.2026.115664

Important note
To cite this publication, please use the final published version (if applicable).
Please check the document version above.

Copyright
In case the licence states “Dutch Copyright Act (Article 25fa)”, this publication was made available Green Open Access via the TU Delft Institutional Repository pursuant to Dutch Copyright Act (Article 25fa, the Taverne amendment). This provision does not affect copyright ownership.
Unless copyright is transferred by contract or statute, it remains with the copyright holder.

Sharing and reuse
Other than for strictly personal use, it is not permitted to download, forward or distribute the text or part of it, without the consent of the author(s) and/or copyright holder(s), unless the work is under an open content license such as Creative Commons.

Takedown policy
Please contact us and provide details if you believe this document breaches copyrights.
We will remove access to the work immediately and investigate your claim.

This work is downloaded from Delft University of Technology.

Optics & Laser Technology 203 (2026) 115664

Contents lists available at ScienceDirect

Optics and Laser Technology

journal homepage: www.elsevier.com/locate/optlastec

Full length article

Emissivity-independent spatiotemporal thermal anomaly detection in metal components using transmission-mode phase measuring deflectometry

Ragni Trivedi [a,1], Shivam Sharma [b,1], Vismay Trivedi [c,*], Rahul Sharma [d], Roger M. Groves [c], Gyanendra Sheoran [b], Arun Anand [d]

[a] Master Programme in Advanced Optical Technologies, Friedrich Alexander University, Konrad-Zuse-Str. 3, 91052 Erlangen, Germany
[b] Advanced Research in Optical and Microwave Applications (AROMA) Lab, Department of Applied Sciences, National Institute of Technology (NIT), Delhi 110036, India
[c] Department of Aerospace Structures and Materials, Delft University of Technology, Kluyverweg 1, 2629 HS Delft, the Netherlands
[d] Optics Laboratory, Department of Physics, Sardar Patel University, Vallabh Vidyanagar, Gujarat 388120, India

ARTICLE INFO

Keywords:
Phase measuringdeflectometry
Thermo-optic effect
Heat-flow mapping
Thermal anomaly detection
Emissivity-independent thermal inspection

ABSTRACT

Non-destructive evaluation of components often relies on infrared thermography, yet metallic and highly conductive surfaces provide weak radiative contrast and require emissivity calibration. We present an emissivity-independent optical approach for rapid spatiotemporal heat-flow mapping and subsurface anomaly detection using transmission-mode phase measuring deflectometry (PMD). A sinusoidal fringe field is imaged through a transparent sensing medium in thermal contact with a thermally stimulated specimen. Thermal diffusion into the sensing medium creates transient temperature gradients; via the thermo-optic effect, these gradients induce refractive-index gradients that modulate the fringe field, enabling an estimation of the temperature-gradient field from the retrieved phase. A coupled experimental–numerical framework is used for quantitative validation: COMSOL-predicted and PMD-derived ROI-averaged vertical temperature-gradient show close agreement over the 0–3 s early-time window, with a root-mean-square error of 0.074 K/mm. Varying the applied thermal load from 5 K to 55 K yields an approximately linear phase response with a system responsivity of 0.0399 rad per unit applied ΔT_{app} (defined between the hot-water reservoir and the imaging chamber at $t = 0$). Demonstrations on representative anomaly classes (dissimilar-material interface, localized low-conductivity insert, and void-type discontinuity) show clear localization of subsurface thermal anomalies within the first few seconds after stimulation, supporting rapid anomaly indication when radiative techniques are constrained.

1. Introduction

Understanding heat flow within materials is essential for applications across energy systems, electronics, aerospace, and advanced manufacturing [1]. Localized deviations in heat transport often reveal structural defects or spatial variations in thermal conductivity, making non-destructive thermal diagnostics crucial for ensuring material integrity [2]. In manufacturing quality assurance, particularly for metallic components, rapid detection of subsurface discontinuities is important for process monitoring, post-process inspection, and in-service screening [3–5]. Optical visualization of heat flow provides a pathway for identifying subsurface anomalies while avoiding surface-emissivity limitations associated with radiative methods [6].

Infrared thermography (IRT) and heat-flow thermography (HFT) are among the most widely used techniques for thermal diagnostics [2,7–9]. However, IRT relies on surface emissivity and performs poorly for metallic or highly conductive surfaces where radiative emission is weak and rapidly varying [10–12]. HFT extends IRT by tracking thermal diffusion but still requires emissivity calibration and high-sensitivity infrared detectors [13–16].

Refractive-index–based optical techniques provide an emissivity-independent route to thermal-field visualization. Classical Schlieren imaging and its digital variants, including background-oriented Schlieren (BOS), respond to refractive-index gradients and are valuable for visualizing large-scale thermal or flow fields [17–22]. Digital holographic interferometry (DHI), in contrast, measures optical-path

* Corresponding author.
E-mail address: vismay.trivedi@gmail.com (V. Trivedi).
[1] These authors contributed equally.

https://doi.org/10.1016/j.optlastec.2026.115664
Received 6 February 2026; Received in revised form 2 May 2026; Accepted 1 June 2026
Available online 4 June 2026
0030-3992/© 2026 The Author(s). Published by Elsevier Ltd. This is an open access article under the CC BY license (http://creativecommons.org/licenses/by/4.0/).

differences with high phase sensitivity but requires coherent illumination, careful alignment, and stringent vibration isolation [23–28].

BOS estimates refractive-index gradients by computing pixel-level displacement fields between a distorted background image and an undisturbed reference [29,30]. While effective with high-contrast artificial backgrounds, its accuracy degrades under small-magnitude refractive-index disturbances, complex natural backgrounds [31], small-scale vortices [32], or varying illumination conditions [33]. These factors limit its suitability for detecting the weak and rapidly evolving temperature gradients encountered in conduction-driven thermal fields within confined geometries. In contrast, transmission-mode phase measuring deflectometry (PMD) analyses phase variations in a high-contrast sinusoidal fringe field, offering higher sensitivity and enabling quantitative retrieval of optical-path gradients within confined transparent media [34].

In practical manufacturing and maintenance settings, conduction-driven thermal signatures are often used in active thermography and related thermal NDE to infer hidden discontinuities [4,35]. This is particularly relevant for metallic components, where infrared inspection can suffer from weak radiative contrast and significant uncertainty due to emissivity variations [36]. Representative scenarios include (i) multi-material or dissimilar-metal regions (e.g., aluminium–steel joints or bimetal assemblies) [37], (ii) localized low-conductivity interlayers or inclusions (e.g., adhesive/bondline defects, insulating inserts, shims, or non-metallic interlayers within a conductive load path) [38,39], and (iii) geometric or material-loss discontinuities such as drilled features, voids, porosity, and occluded cavities that perturb heat-flow pathways and produce detectable thermal anomalies [35,40]. These three classes are intentionally represented by the test specimens used here (Objects 1–3), providing an application-oriented baseline for rapid anomaly screening under controlled thermal loading [35].

PMD offers a compact, alignment-tolerant, and emissivity-independent approach for visualizing refractive-index gradients in transparent media. PMD measures angular deflections of structured-light fringes, enabling reconstruction of optical-path variations [34,41,42]. Although originally developed for surface-shape metrology, recent extensions have demonstrated its applicability to refractive-index imaging, including microscopic profiling of transparent micro-objects [43], refractive-index estimation of liquids [44], and qualitative heat-flow visualization in metals [45].

Building on these developments, the present work advances PMD from qualitative visualization toward quantitative thermal-field mapping by correlating measured PMD phase gradients with numerically simulated temperature gradients. In the proposed configuration, heat diffuses from a thermally loaded metallic specimen through a thin aluminium foil into a transparent medium, where conduction establishes refractive-index gradients that distort the imaged fringe pattern. A coupled experimental–numerical framework is implemented: PMD records the dynamic phase evolution, while a COMSOL model computes the corresponding transient temperature gradients. Their agreement demonstrates that PMD can retrieve quantitative thermal-gradient information, enabling compact and calibration-ready thermal-metrology systems that rely on optical sensing while using contact-mediated heat transfer.

2. Theoretical background

Transmission-mode phase measuring deflectometry (PMD) measures angular deflections of light rays caused by spatial variations in refractive index within a transparent medium, which appear as distortions of an imaged sinusoidal fringe pattern [46]. In the present work, the fringe pattern is imaged through a sensing medium with temperature-dependent refractive index. Heat conducted into this medium establishes transient temperature gradients, which induce refractive-index gradients via the thermo-optic effect. These gradients bend rays and cause measurable displacements (distortions) in the recorded fringe pattern [46–48].

In transmission-mode PMD, ray bending can be interpreted as refraction in a medium with spatially varying optical thickness: rays deviate toward regions of higher optical path length, and the corresponding deflection is governed by optical-thickness gradients transverse to the optical axis [46]. Practically, PMD quantifies this effect by analysing the change in the imaged fringe pattern between a reference state and a thermally disturbed (object) state, recorded using a display–lens–camera configuration [34]. The retrieved phase is proportional to the angular deflection and therefore to the gradient of optical thickness perpendicular to the fringe orientation; absolute optical thickness can be obtained by integrating the measured gradients over the field [49]. Several fringe-analysis algorithms exist for recovering the phase from the recorded fringe pattern. Fourier-transform fringe analysis is particularly robust and computationally efficient for PMD applications [50].

Under the small-angle approximation, the local deflection angle α is proportional to the lateral gradient of optical thickness S along the PMD sensitivity direction (here taken as y) [46–48]:

$$\alpha \propto \frac{\partial S}{\partial y} \tag{1}$$

The y-direction is selected because the thermal stimulus is applied approximately as a planar heat source, so the dominant heat flow and hence the maximum temperature gradient in the sensing medium is expected to be normal to the heated interface (along y). With $= nL$, where n is the refractive index and L is the physical thickness of the medium along the optical axis (i.e., the effective optical path length through the medium), the presence of a thermal gradient gives

$$\frac{\partial S}{\partial y} = L\frac{\partial n}{\partial y} = \mu L\frac{\partial T}{\partial y} \tag{2}$$

where $\mu = \frac{dn}{dT}$ is the thermo-optic coefficient of the medium.

A sinusoidal pattern is displayed on an LCD screen and recorded by a lens-camera system. First the reference intensity distribution $I_{ref}(x,y)$ is captured with the medium at uniform temperature (or without thermal loading),

$$I_{ref}(x,y) = I_0(x,y) + I_1(x,y)cos\left[\varphi_{ref}(x,y)\right] \tag{3}$$

where $I_0(x,y)$ and $I_1(x,y)$ are the background and modulation terms, respectively, and $\varphi_{\mathrm{ref}}(x,y)$ is the total phase of the fringe pattern at the camera plane. When the object is imaged through the heated sensing medium, the corresponding object intensity distribution $I_{\mathrm{obj}}(x,y)$ becomes [51]

$$I_{obj}(x,y) = I_0(x,y) + I_1(x,y)cos\left[\varphi_{obj}(x,y)\right] \tag{4}$$

The total phase term in each case can be decomposed into a geometry-dependent carrier contribution and a local phase modulation:

$$\varphi_k(x,y) = \frac{2\pi d}{p}\alpha + \phi_k(x,y), k \in \{ref, obj\} \tag{5}$$

where d is the distance between the displayed fringe pattern and the phase object, p is the fringe period, and α is the local ray deflection angle along the sensitivity direction. For small deflections ($\alpha \ll 1rad$), $\sin\alpha \approx \alpha$. The term $\phi_k(x,y)$ represents the local phase modulation associated with the refractive-index gradients in the medium for the reference (k = ref) and object (k = obj) states.

A phase-extraction algorithm (e.g., phase-shifting or Fourier fringe analysis) is applied separately to $I_{\mathrm{ref}}(x,y)$ and $I_{\mathrm{obj}}(x,y)$ to retrieve the corresponding phase maps $\phi_{\mathrm{ref}}(x,y)$ and $\phi_{\mathrm{obj}}(x,y)$. The PMD phase shift due to thermal loading is then defined as

$$\Delta\phi(x,y) = \phi_{obj}(x,y) - \phi_{ref}(x,y) \tag{6}$$

which isolates the contribution of the thermally induced refractive-index gradient and removes static system aberrations.

Combining Eqs. (1) and (2) with the geometric sensitivity of the fringe pattern, the phase shift can be written as [34,46,50],

$$\Delta\phi = \frac{2\pi d}{p}\frac{\mu L}{n_0}\frac{\partial T}{\partial y} \tag{7}$$

where n_0 is the refractive index of the medium at the reference temperature, L is the physical thickness of the sensing medium, and $\partial T/\partial y$ is the temperature gradient along the sensitivity direction. Eq. (7) defines the proportionality constant $= \frac{2\pi d}{p}\frac{\mu L}{n_0}$, which links the experimentally measured phase shift to the underlying temperature gradient. This relation is used later (Section 4) to compute the predicted PMD phase shift from simulated temperature gradient and to enable a direct comparison with the experimentally retrieved phase-shift maps in Section 5.

To retrieve phase maps, Fourier-transform fringe analysis is employed [50] where the Fourier spectrum of the recorded fringe intensity (Eq. (3) or (4)) is filtered around a first-order lobe to form an analytic signal whose argument yields the wrapped phase, which is then unwrapped using a standard two-dimensional phase-unwrapping algorithm. The resulting $\Delta\phi(x,y)$ is therefore proportional to the local temperature gradient via Eq. (7).

To visualize heat flow in opaque and diffusely scattering materials, the test object is placed in thermal contact with a transparent sensing medium (Fig. 1). Thermal anomalies within the object perturb heat flow into the sensing medium, producing localized variations in $\partial T/\partial y$ and corresponding anomalies in $\Delta\phi(x, y)$, enabling subsurface anomaly visualization through the refractive-index response of the coupled transparent layer.

3. Experimental setup

Fig. 2 provides an overview of the transmission-mode PMD system and the thermal-loading arrangement used for heat-flow mapping and anomaly detection.

3.1. Test objects and anomaly cases

Three test objects were designed to represent distinct classes of thermal anomalies relevant to defect detection. The anomaly types and corresponding specimen constructions are summarized in Table 1. In brief, Object 1 evaluates discrimination between two materials with different thermal conductivities, Object 2 represents a localized discontinuity smaller than the overall object size, and Object 3 represents a subsurface discontinuity embedded within the bulk.

Preliminary transient heat-conduction simulations were used to guide the experimental design by indicating (i) the time window during which anomalies remain detectable and (ii) the thermal contrast required for clear discrimination between nominal and perturbed regions. The simulations also showed that a spatially uniform, high-flux thermal stimulus improves anomaly visibility. Accordingly, a hot-water reservoir was selected as the thermal probe, as it provides a nearly uniform and sustained heat input. Further simulation details are provided in Supplement 1.

3.2. PMD measurement system

The experimental setup used for transmission-mode PMD–based thermal mapping consists of three primary components: (i) the fringe-display unit, (ii) the sensing unit (imaging chamber), and (iii) the imaging unit. A schematic of the arrangement is shown in Fig. 2(a–b), and a photograph of the implemented system is provided in Fig. 2(c).

The fringe-display unit consists of a high-resolution TFT–LCD screen (1080 × 1920 pixels, 403 PPI, 800 nits), which displays a sinusoidal fringe pattern. The fringe period is chosen to be 0.7 line pairs/mm, and the pattern is oriented at 45° so that both x- and y-components of the optical-path gradient contribute to the measured phase. This oblique orientation eliminates the need for separate measurements with horizontal and vertical fringes and enables efficient two-dimensional sensitivity. The LCD display allows flexible adjustment of fringe frequency and orientation to tune the measurement sensitivity for different samples.

The sensing unit comprises a transparent imaging chamber filled with distilled water, enclosed by 1.5 mm thick glass walls. The top of the chamber is sealed using a thin aluminium foil (≈ 200μm), which acts as the thermal interface between test object and water of the imaging chamber. The test object is placed directly above the foil. When a thermal load is applied to the object, heat conducts into the water-filled chamber, producing refractive-index gradients that distort the imaged fringe pattern. Water is selected as the sensing medium due to its relatively high thermo-optic coefficient, good optical clarity, and ease of handling. Other transparent media (e.g., acrylic, glass, silicone oils) can be used to tailor sensitivity for specific applications.

The imaging unit consists of a CCD camera (768 × 1024 pixels, 8-bit, 4.65 μm pixel pitch) equipped with a 25-mm focal-length lens. The camera is positioned to directly image the displayed fringe pattern through the sensing chamber. From the system geometry, the overall

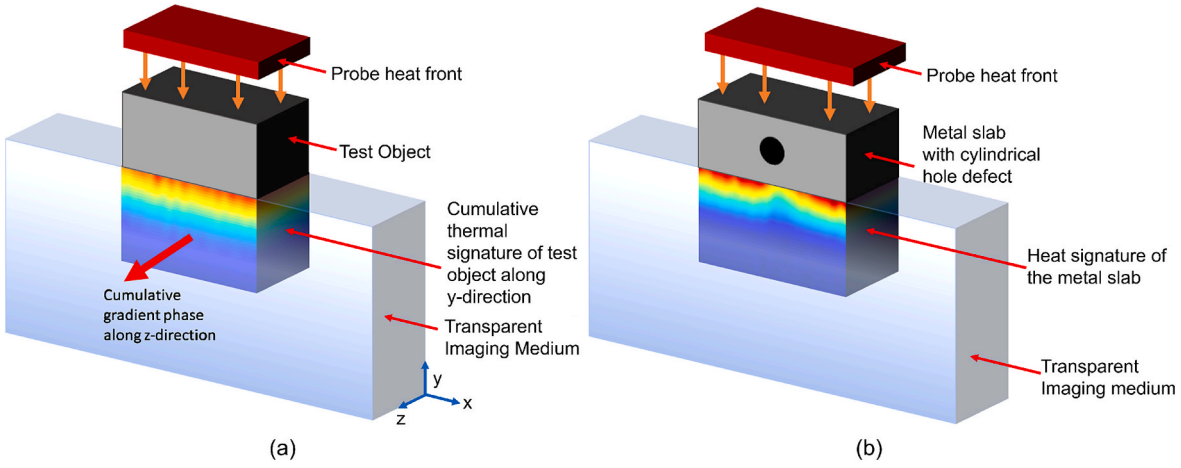

Fig. 1. Principle of anomaly detection using transmission-mode PMD. (a) Heat flows from the opaque test object into the transparent sensing medium through a thin aluminium foil, producing refractive-index gradients. (b) These gradients distort the fringe pattern, generating a PMD phase map that reveals subsurface thermal anomalies.

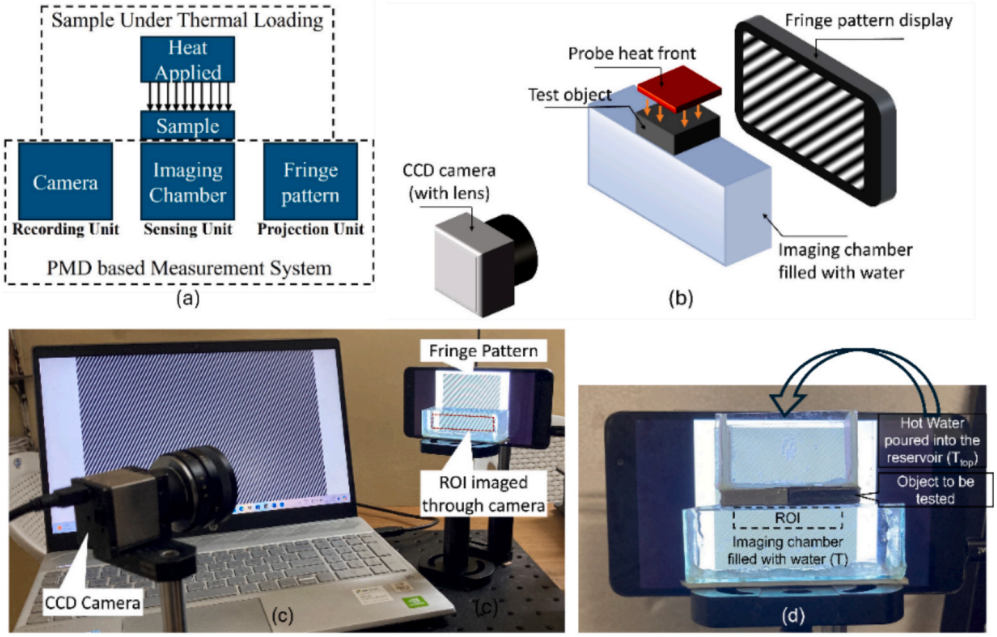

Fig. 2. Experimental setup for PMD-based thermal-field mapping. (a) Block diagram of the complete system. (b) Schematic of the imaging chamber, fringe display, and camera geometry. (c) Photograph of the table-top implementation with the region of interest (ROI). (d) Thermal loading of the test object using a hot-water reservoir at temperature T_{top}, producing a uniform heat pulse.

Table 1
Description of test objects and thermal anomalies they are designed to represent.

Sr. No.	Type of thermal anomaly	Description of the test object	Diagram
Object 1	Distinguishing between two materials of different thermal conductivity	Two slabs of Aluminium (Al) and Structural Steel (SS) of dimension 25 mm x 25 mm x 5 mm each placed side by side	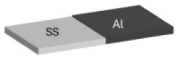
Object 2	Identifying thermal discontinuity relatively smaller than the object in which it is present	Glass slab (25 mm x 1 mm x 5 mm) placed between two aluminium slabs (25 mm x 25 mm x 5 mm)	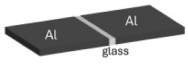
Object 3	Identifying thermal discontinuities situated well within the bulk object	SS slab (25 mm x 25 mm x 6 mm) with a centrally located hole of diameter 3 mm oriented through thickness	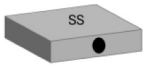

optical demagnification factor is approximately 0.082.

3.3. Thermal excitation, acquisition, and processing

Thermal excitation is applied using a hot-water reservoir maintained at T_{top}, delivering an approximately uniform thermal load to the upper surface of the test object (Fig. 2(d)). A reference fringe image is acquired with the system at the initial uniform temperature T_0. After thermal loading begins, a time-resolved sequence of fringe images is recorded at 30 fps for 10 s to capture the evolution of refractive-index gradients generated by heat flow from the object into the sensing medium. Recorded fringe images are processed using Fourier-transform fringe analysis (Supplement 1). The reference phase is subtracted from the heated-state phase to isolate the thermally induced component, yielding time-resolved phase-shift maps. Using the phase–temperature-gradient relation derived in Section 2 (Eq. (7)), these phase maps are converted to temperature-gradient fields within the sensing medium. The resulting spatiotemporal maps form the basis for heat-flow visualization and for identifying localized perturbations associated with thermal anomalies (Section 5).

4. Numerical simulation

To support the interpretation of defect signatures and to enable quantitative validation against experiments, two complementary simulation approaches were employed. ANSYS Workbench was used as a screening model to study how different anomaly classes (Objects 1–3) perturb the transient heat-flow field under a planar thermal stimulus. COMSOL Multiphysics was used as a quantitative model to replicate the full experimental configuration and to predict the temperature gradients within the sensing medium that give rise to the measured PMD phase response for the homogeneous aluminium-slab validation case.

4.1. ANSYS screening simulations for thermal signature prediction

Three-dimensional transient heat conduction was simulated in ANSYS Workbench 2023 R2 (Student Version) for the three test objects described in Table 1. A spatially uniform (planar) thermal stimulus was applied to the loading surface, and the resulting spatiotemporal temperature fields were analysed to identify characteristic thermal signatures expected for each anomaly type. The governing heat-conduction model follows the Fourier–Biot equation [52]:

$$\frac{\partial}{\partial x}\left(k\frac{\partial T}{\partial x}\right)+\frac{\partial}{\partial y}\left(k\frac{\partial T}{\partial y}\right)+\frac{\partial}{\partial z}\left(k\frac{\partial T}{\partial z}\right)+q_v=\rho c_p\frac{\partial T}{\partial t} \tag{8}$$

here ρ, c_p, and k are the density, specific heat, and thermal conductivity, respectively, and q_v is the volumetric heat-generation term. These simulations are used to support the qualitative interpretation of anomaly-induced perturbations; detailed settings and representative field plots are provided in Supplement 1.

4.2. COMSOL model for quantitative comparison and phase prediction

A numerical model was developed in COMSOL Multiphysics 6.2 to replicate the experimental configuration and to predict the transient temperature field that drives refractive-index gradients in the sensing medium and hence the PMD phase response. The geometry comprised an upper water chamber (21 mm × 26 mm × 24 mm) acting as the heat reservoir, an aluminium slab representing the test object (24 mm × 6 mm × 27 mm), a lower water chamber (86 mm × 26 mm × 24 mm) representing the sensing volume, and glass walls of 1.5 mm thickness enclosing both chambers. All domains were embedded in an air box representing the laboratory environment (Fig. 3). The thermophysical properties used for each material are listed in Table 2.

The initial temperatures were prescribed to match the experimental boundary conditions used for validation, with the hot-water reservoir at $T_{top} = 303.15K$ and the sensing chamber initially at $T_0 = 298.15$ K. The air inside the enclosing air box was initialized at 303.15 K. Heat exchange at the outer boundary of the air domain was modeled using a convective boundary condition with an external ambient temperature $T_\infty = 308.15K$ and a uniform heat transfer coefficient $h = 5Wm^{-2}K^{-1}$, representing weak natural-convection coupling at the enclosure boundary. Because the present comparison focuses on the initial 0–3 s heating window, the PMD-relevant ROI gradients are dominated by heat transfer through the object–interface–sensing-medium stack, while moderate variations in h primarily influence slower ambient exchange.

The chosen value therefore provides a physically reasonable approximation of ambient coupling while preserving the conduction-dominated behaviour relevant to the measurement. Gravity was included along the negative y-direction to account for natural convection within the fluid regions (air and water). A transient heat-transfer simulation was performed, and the temperature field was analysed over the first 3 s to correspond to the time window of interest in the experiment.

4.3. Region of interest and extraction of representative gradients

The simulation indicates that the applied thermal stimulus is approximately planar at the top surface of the specimen; consequently, the dominant heat flux propagates along the y-direction into the lower water chamber. To enable direct comparison with the PMD measurements, all quantitative comparisons are restricted to the 0–3 s early-time window, which captures the initial conduction-dominated response responsible for establishing measurable refractive-index gradients in the sensing medium. Over this interval, the ROI-averaged vertical temperature gradient $\langle \partial T/\partial y \rangle(t)$ exhibits a well-defined transient maximum and then evolves as boundary exchange and the decay of the driving thermal load begin to influence the response. The simulated temperature-gradient field is used together with Eq. (7) to predict the corresponding PMD phase response, providing the forward model for the experimental validation in Section 5.1.

Table 2
Thermophysical properties of materials used in the COMSOL simulations.

Material	Density (kg/m^3)	Thermal Conductivity (W/m·K)	Specific Heat (J/kg·K)	Dynamic Viscosity (Pa·s)	Source
Water	998	0.6	4180	0.001	COMSOL default
Aluminium	2700	205	900	–	Standard values [53]
SiO_2 (Glass)	2200	1.38	703	–	Standard values [53]
Air	1.2	0.026	1005	1.8×10^{-5}	COMSOL default

For a quantitative comparison with the measurements, the temperature field was evaluated over a region of interest (ROI) beneath the test object. In the numerical model, this ROI was defined as a cuboid of dimensions 20 mm × 2 mm × 21 mm along the x-, y-, and z-directions, respectively. The lateral dimensions (20 mm × 2 mm) were chosen to approximately match the experimentally imaged ROI used during PMD post-processing, which is inherently two-dimensional. The additional extent in the third direction (21 mm) was included to capture the full three-dimensional heat transport within the sensing volume.

To quantify the representative vertical temperature gradient, the ROI was discretized into a series of parallel sheets along the y-direction with a spacing of $\Delta y = 0.1mm$. The average temperature was computed for each sheet, yielding 20 sheet-averaged temperatures $T_1, T_2, \cdots, T_{20}$, where T_1 corresponds to the sheet closest to the slab-side interface. A set of average (secant) gradients was then computed with respect to this reference sheet as $g_i = \frac{T_1 - T_i}{(i-1)\Delta y}$, $i = 2,\ldots,20$ and the representative vertical temperature gradient within the ROI was taken as the mean of g_i over all sheets. This approach provides a robust macroscopic estimate by averaging over multiple gradient evaluations, thereby reducing sensitivity to small-scale numerical noise. Furthermore, the use of sheet-averaged temperatures is consistent with PMD measurements, which inherently integrate refractive-index variations over finite imaging regions rather than resolving pointwise values. Thus, the methodology establishes a direct and physically meaningful link between the simulated temperature field and the experimentally observed phase contrast.

Within this ROI, the vertical temperature gradient $\partial T/\partial y$ is clearly dominant, whereas the gradients along the in-plane directions $\partial T/\partial x$ and

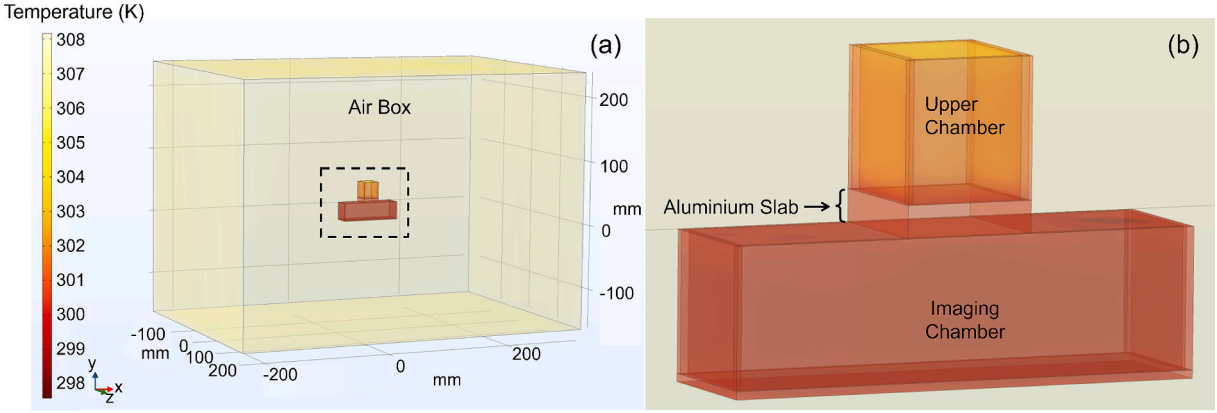

Fig. 3. COMSOL geometry used for simulating transient heat transfer. (a) Air domain enclosing all components used in the PMD experiment; the colorbar illustrates a representative simulated temperature field (K) used for visualization of the simulation geometry and thermal loading configuration. (b) Enlarged view showing the upper water chamber (heat reservoir), aluminium slab, lower water chamber (sensing volume), and glass walls.

$\partial T/\partial z$ remain comparatively small. This behaviour follows from the applied boundary conditions: the principal heat flux is directed normal to the slab surface, leading to predominantly one-dimensional heat flow through the thickness, while lateral temperature variations are smoothed out by diffusion. The sign and magnitude of $\partial T/\partial y$ confirm that heat is transferred from the upper hot-water reservoir toward the lower glass wall of the imaging chamber, generating the refractive-index gradient responsible for the measured PMD phase shift.

5. Experimental results and discussion

5.1. Dynamic response, comparison with simulation, and responsivity

To enable a direct quantitative comparison with the COMSOL model, an experiment was performed with the hot-water reservoir maintained at $T_{top} = 303.15$ K and the imaging chamber at $T_0 = 298.15$ K, corresponding to an applied temperature difference $\Delta T_{app} = 5$ K, identical to the simulation condition. The ambient conditions were controlled using air conditioning; the imaging-chamber temperature was monitored with a standard thermometer and stabilized at the target initial value before each measurement. A homogeneous aluminium block (25 mm × 25 mm × 6 mm) was used as the test specimen for this validation measurement.

Fig. 4(a) shows the time evolution of the ROI-averaged vertical temperature gradient, $\langle \partial T/\partial y \rangle(t)$, comparing the COMSOL prediction with the gradient estimated from the measured PMD phase using Eq. (7). Fig. 4(b) shows the corresponding evolution of the ROI-averaged PMD phase shift in the vertical sensitivity direction, $\langle \Delta\phi(t) \rangle$. To reduce the influence of measurement noise, the experimental gradient curve was obtained by repeating the $\Delta T_{app} = 5$K experiment multiple times and averaging the phase-derived gradients prior to comparison with COMSOL.

A quantitative measure of agreement is the global RMSE between the experimental and simulated $\partial T/\partial y(t)$ curves over 0–3 s. Over this interval, RMSE = 0.074 K/mm, which is ~ 10% of the peak experimental gradient magnitude, indicating good agreement for a proof-of-concept transient thermo-optic measurement. Minor deviations are expected due to practical uncertainties in initial/boundary conditions and simplified modelling of convective exchange.

The purpose of the COMSOL–experiment comparison is to demonstrate that the proposed sensing configuration and the forward model reproduce the initial conductive heating response that is most relevant to rapid inspection. During this early window (here taken as 0–3 s), the PMD-relevant gradients in the ROI are dominated by heat transfer through the object–interface–sensing-medium stack, making this interval appropriate for quantitative comparison. This interval also corresponds to the time range in which detectable anomaly signatures first appear, which is important for rapid identification. At later times, additional effects (e.g., convective exchange with the surroundings, evolving boundary interactions, and decay of the thermal driving force as the hot-water probe cools) increasingly influence the transient response and can introduce case-dependent cooling behaviour. Therefore, the quantitative validation is intentionally restricted to the first 3 s, where the physics is conduction-dominated and most directly linked to the measured phase response. Once agreement is established in this window, COMSOL outputs can be used with greater confidence to support interpretation and calibration in the remainder of the study. The hot-water reservoir is used to create a quick and approximately uniform planar thermal load at the start of this transient phase. Beyond the early-time validation window, the response remains qualitatively interpretable as a continuation of the early-time heat-flow process, but is not used for precise quantitative comparison with the COMSOL model.

To further investigate the response of the system to different thermal inputs, a second set of experiments was performed by varying the applied thermal load on the aluminium block. The temperature of the top water reservoir was increased from 303.15 K to 353.15 K in steps of 10 K, while the imaging-chamber temperature was maintained at 298.15 K. This produced applied temperature differences ΔT ranging from 5 K to 55 K.

For the $\Delta T = 5$ K experiment, the actual temperature rise within the field of view during the initial heating stage is small, typically around or below 1 K, and evolves rapidly over a few seconds. Conventional temperature measurement techniques such as thermocouples or infrared cameras do not provide the required combination of spatial and temporal resolution to capture these fast, low-magnitude variations. As this work is a proof-of-concept study, COMSOL-derived temperature fields are therefore used to interpret the measured thermal gradients and to validate the observed PMD phase shifts under controlled boundary conditions.

Accordingly, the externally applied temperature difference (between the hot-water reservoir and the imaging chamber at $t = 0$) is used as the reference input for defining the system responsivity. For each applied thermal load, the ROI-averaged PMD phase was computed, and the resulting phase-versus-ΔT curve (Fig. 5) exhibits an approximately linear trend. From the slope of this curve, a responsivity of 0.0399 rad per unit applied ΔT was obtained. This quantity characterizes how strongly the measured phase responds to changes in the applied thermal load within the investigated operating range; it should not be interpreted as a direct physical sensitivity in rad/K to the internal ROI temperature change.

The responsivity of the system is defined as the slope of the ROI-

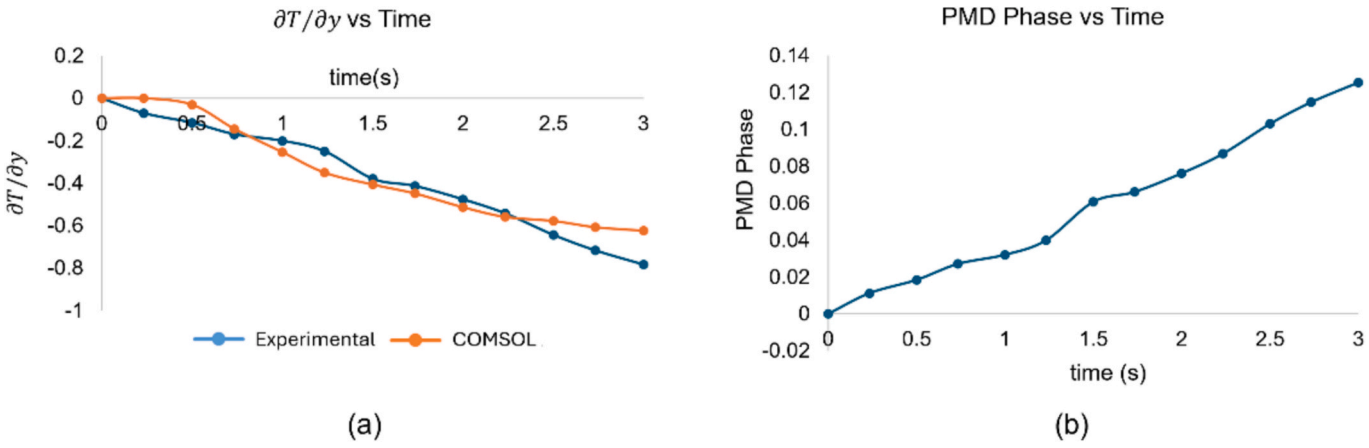

Fig. 4. Dynamic response of the PMD system for an applied $\Delta T = 5$ K. (a) ROI-averaged vertical temperature gradient estimated from PMD phase via Eq. (7) compared with COMSOL prediction. (b) Corresponding mean PMD phase in the same ROI. The experimental gradient curve is obtained from repeated measurements averaged prior to comparison.

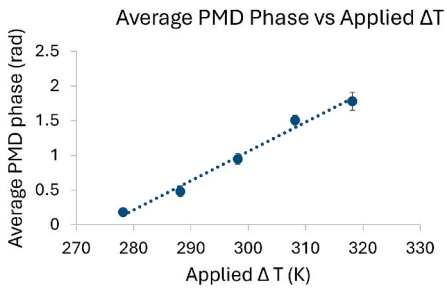

Fig. 5. Responsivity curve: ROI-averaged PMD phase shift as a function of applied temperature difference ΔT. The slope yields the system responsivity in rad per unit applied ΔT.

averaged PMD phase shift with respect to the applied thermal load $R_{\phi,\Delta T} = \frac{d<\Delta\phi>_y}{d(\Delta T)}$ rad per K of applied ΔT, where ΔT denotes the difference between the hot-water reservoir and the imaging chamber at $t = 0$. This definition uses ΔT_{app} as a surrogate input because direct, spatially resolved measurement of the small, rapidly evolving internal temperature change within the ROI is not feasible with conventional sensors at the required spatiotemporal resolution in the present proof-of-concept setup. Accordingly, $R_{\phi,\Delta T_{\text{app}}}$ should be interpreted as a system-level responsivity of the overall sensing configuration to the applied thermal stimulus (units: rad per unit applied ΔT_{app}), rather than an intrinsic rad/K sensitivity to the local ROI temperature.

In addition to this system-level metric, the intrinsic sensitivity linking the measured PMD phase shift to the local vertical temperature gradient in the sensing medium is given by Eq. (7), $\Delta\phi = K(\partial T/\partial y)$, where K is set by the optical geometry and the thermo-optic response of the sensing medium. Since the thermo-optic gradients are distributed throughout the water depth, d is defined using an effective phase plane located within the sensing volume (rather than at a single glass interface). With this effective definition, the resulting geometric constant is $K \approx -1.6 \times 10^{-4}\text{rad}/(\text{K/m})$. This constant is used to relate simulated temperature gradients to the expected PMD phase response and to support comparison between COMSOL predictions and PMD measurements.

5.2. Spatiotemporal thermal mapping and anomaly detection

A second set of experiments demonstrates thermal anomaly detection for the three objects described in Table 1. In the present work, "anomaly detection" refers to the detection and localization of thermal anomalies through spatially resolved phase variations, rather than criterion-based defect segmentation. The known positions of the material interfaces, low-conductivity insert, and void-type discontinuity provide a direct reference for interpreting the measured phase maps and line profiles where clear local deviations from the surrounding regions are observed. However, accuracy measures such as segmentation accuracy, error in estimated defect area, or overlap-based metrics are not the focus of the present study and would require an additional analysis framework involving objective threshold selection, ground-truth defect masks, and validation across a wider range of defect sizes, depths, and geometries. In each test, the object was placed on the imaging chamber (water initially at ambient temperature), and a thermal probe was applied using hot water (Fig. 2). The spatiotemporal PMD phase maps presented below reflect the evolving refractive-index gradients in the sensing medium and are therefore proportional to the temperature-gradient field (Eq. (7)).

Fig. 6 shows the PMD phase maps obtained for Object 1 (Table 1) for an imaging-chamber temperature of $T_c = 298.15\text{K}$ and a hot-water (probe) temperature of $T_p = 336.15$ K, corresponding to an applied temperature difference $\Delta T_{\text{app}} = T_p - T_c = 38\text{K}$. Here, $t = 0$ denotes the instant when the hot water first contacts the upper surface of the specimen.

Because aluminium has substantially higher thermal conductivity (and thermal diffusivity) than structural steel, the heat front propagates more rapidly and produces a larger phase response on the aluminium side, making the material interface detectable as a spatial discontinuity in the phase field. To visualize the evolution more clearly, the phase profile is evaluated along a horizontal line (along x) crossing the interface, as indicated by the dashed line in Fig. 6(c). Since the dominant heat

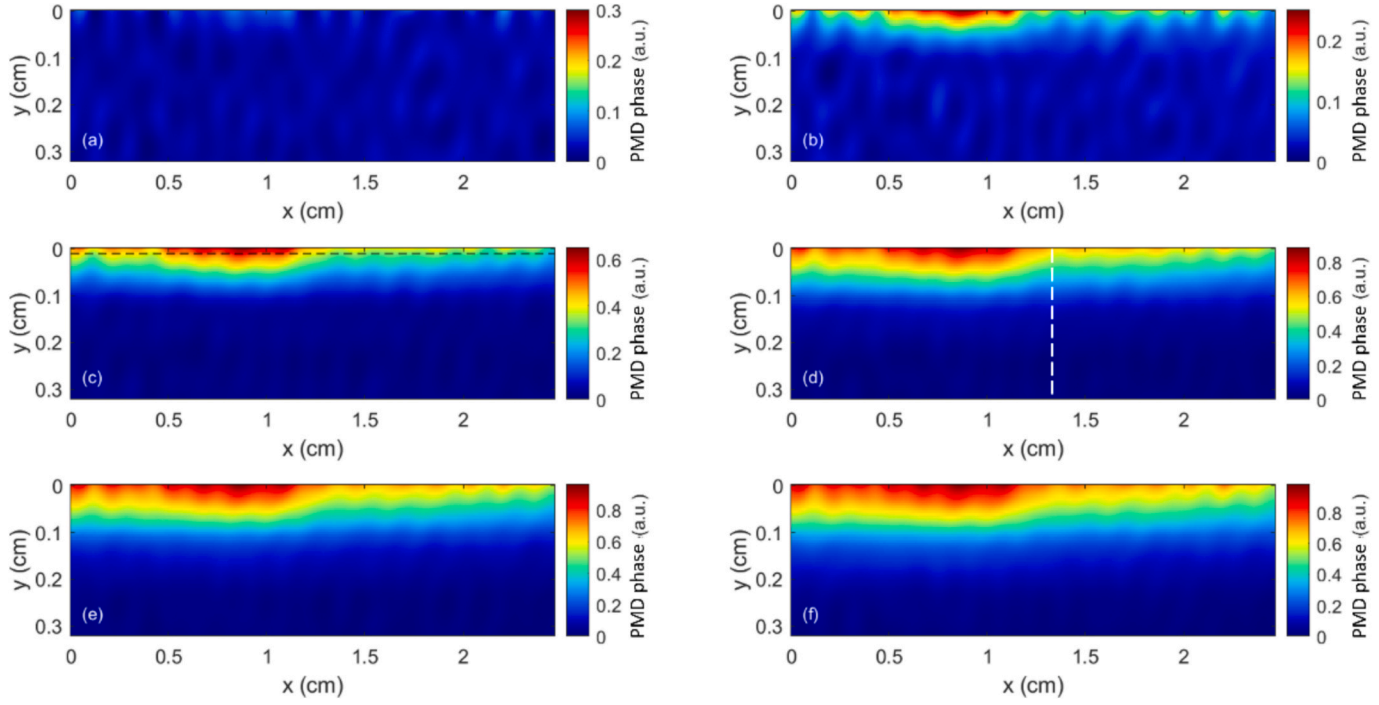

Fig. 6. Spatiotemporal evolution of the PMD phase map (proportional to the vertical temperature gradient) for Object 1. Times: (a) 0.40 s, (b) 0.87 s, (c) 1.87 s, (d) 2.87 s, (e) 3.67 s, (f) 4.67 s. Aluminium and Structural steel regions produce distinct thermal signatures due to differing thermal conductivities. (See Visualization 1.).

flow is along the *y*-direction in this configuration, this lateral profile highlights the contrast between the two materials. Fig. 7(a–f) shows the corresponding phase profiles at successive times. A distinct interface signature becomes apparent approximately $\sim 1s$ after application of the thermal load.

The phase on the Al side increases more rapidly and reaches higher values than on the SS side, consistent with faster heat propagation through aluminium. The interface location is indicated by the vertical dotted line in Figs. 6 and 7.

Fig. 8 presents the PMD phase maps obtained at different times for Object 2 (Table 1) with an imaging-chamber temperature of T_c = 298.15 K and a hot-water (probe) temperature of T_p = 328.15 K, corresponding to an applied temperature difference $\Delta T_{app} = T_p - T_c = 30$ K. Object 2 consists of a glass slab placed between two aluminium slabs.

Because aluminium has a much higher thermal conductivity (and thermal diffusivity) than glass, the heat front propagates more rapidly through the aluminium regions, whereas the glass segment retards conduction and alters the local heat-flow pathways. This strong thermal-transport contrast produces a non-uniform temperature field and a clear discontinuity in the PMD phase distribution across the insert region.

As the hot-water probe is not actively maintained, the thermal driving force decreases with time and the imaging-chamber water gradually approaches thermal equilibrium. Consequently, temperature differences between regions diminish and the phase contrast reduces as the field becomes increasingly uniform, eventually obscuring finer anomaly details at later times. Fig. 9(a–f) shows the corresponding PMD phase profiles along the dashed line indicated in Fig. 8(c), further illustrating the reduced phase response over the glass segment relative to the adjacent aluminium regions. Compared with the aluminium–structural steel interface case (Object 1), the aluminium–glass–aluminium configuration introduces a much larger thermal-property contrast, which yields a clearer anomaly signature; however, the low-conductivity glass region also delays heat penetration, so the signature typically evolves over a longer transient before homogenization dominates. Together, Figs. 8 and 9 demonstrate that the technique can detect localized variations in thermal conductivity and is therefore suitable for identifying defect-like thermal discontinuities and material inhomogeneities.

Fig. 10 shows the PMD phase maps obtained at different times for Object 3 (Table 1) for an imaging-chamber temperature of T_c = 298.15K and a hot-water (probe) temperature of T_p = 353.15K , corresponding to an applied temperature difference $\Delta T_{app} = T_p - T_c$ = 55K. Here, $t = 0$ denotes the instant when the hot water first contacts the upper surface of the specimen. Object 3 is a structural steel slab containing a cylindrical void; the void perturbs heat-flow pathways and locally reduces conductive heat transfer relative to the surrounding solid material. As a result, the PMD phase response above the void region differs from that of the adjacent intact structural steel.

This behaviour is evident in Fig. 10(b), where the phase field exhibits a distinct spatial deviation above the cylindrical hole compared with the surrounding region. The variation observed along the *x*-direction arises from changes in the dominant heat flow along the *y*-direction caused by the subsurface discontinuity. Fig. 11(a–f) shows the corresponding PMD phase profiles extracted along the dashed line indicated in Fig. 10(c), further highlighting the reduced phase response associated with the void. Since the host is fully metallic, the heat front develops rapidly in the intact regions, and the void-induced perturbation becomes detectable within the first few seconds of heating.

The time at which a detectable phase signature appears is governed by two factors: (i) the magnitude of the thermal-property contrast that creates spatial differences in heat flow, and (ii) the rate at which the heat front develops within the specimen. For Object 1 (Al–SS), both regions are metals, so the thermal contrast is moderate; the interface becomes detectable after a short delay (≈1 s), but the phase contrast is relatively modest compared with Object 2. For Object 2 (Al–glass–Al), the conductivity/diffusivity mismatch is much larger, producing a clearer discontinuity; however, the low-conductivity glass insert also delays heat penetration, so the anomaly signature evolves over a longer transient before diffusion and probe cooling reduce contrast. For Object 3 (SS with a void), heat transport in the intact metal is fast, and the void perturbs the conduction pathway strongly, so a localized deviation becomes visible within the first seconds of heating.

The spatiotemporal evolution of the PMD phase maps for all three objects is provided in the supplementary visualization files. In all cases, the PMD phase increases with time, reaches a maximum, and then decreases. This trend reflects the nature of the thermal probe: the hot water

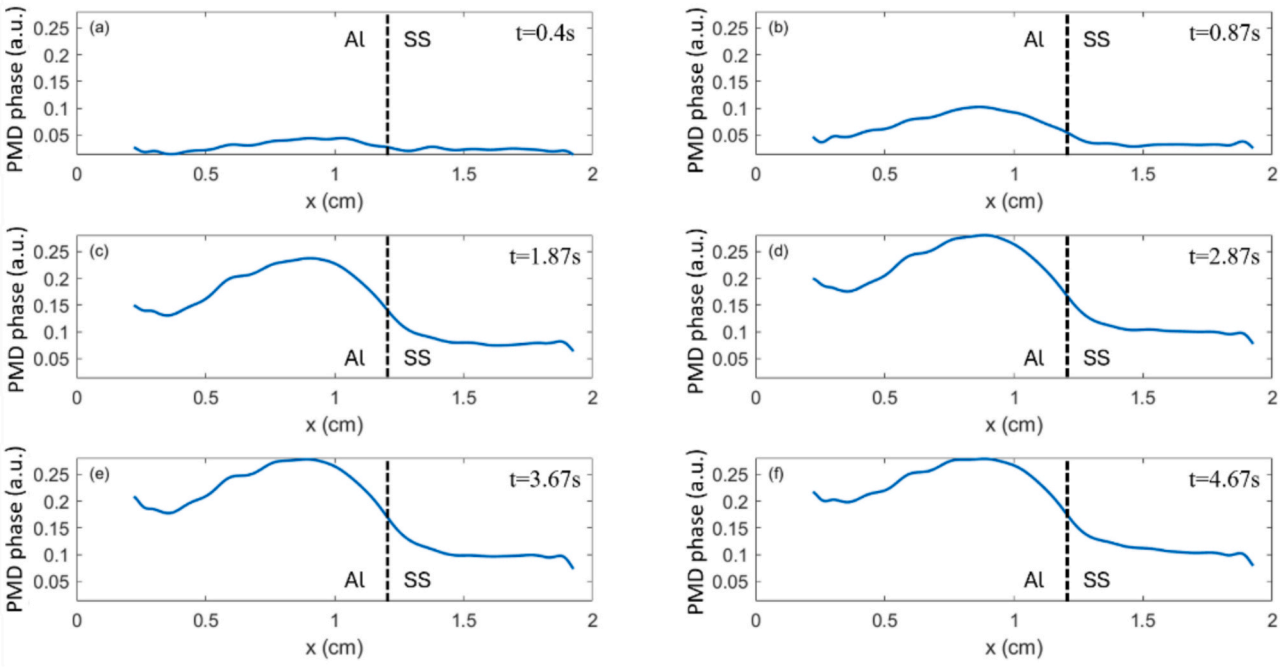

Fig. 7. Temporal evolution of the PMD phase profile along the dashed horizontal line in Fig. 6(c), illustrating the progression of the heat front through aluminium and structural steel.

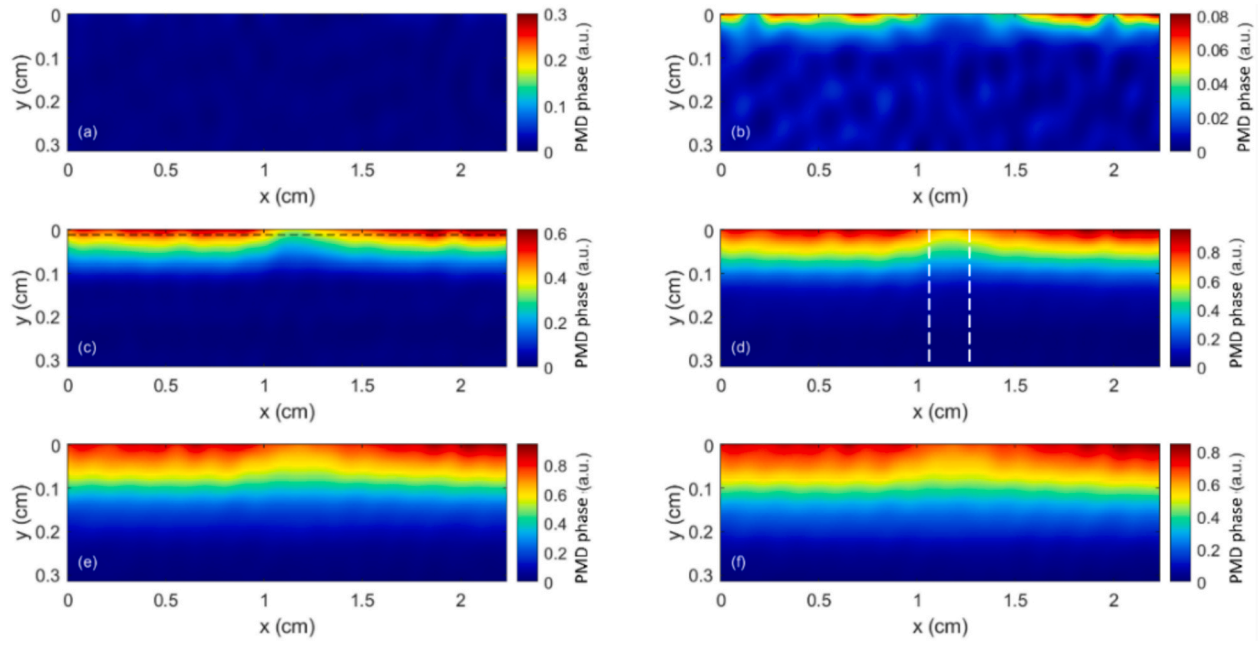

Fig. 8. Spatiotemporal evolution of the PMD phase map for Object 2, containing a glass insert between aluminium slabs. Times: (a) 0.40 s, (b) 0.60 s, (c) 1.80 s, (d) 3.13 s, (e) 5.47 s, (f) 7.13 s. Thermal conduction slows through the glass region, producing a clear thermal discontinuity. (See Visualization 2.).

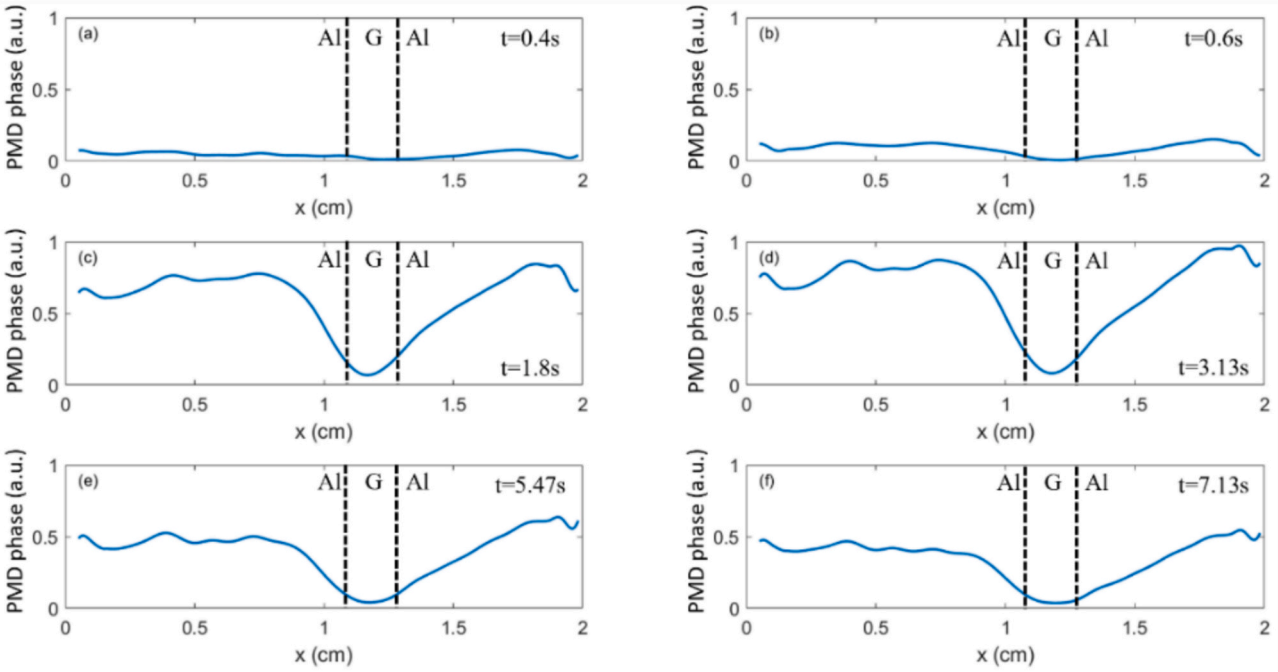

Fig. 9. PMD phase profiles along the dashed line in Fig. 8(c), highlighting slower heat propagation through the glass insert relative to the surrounding aluminium.

loses heat to both the object and the surroundings, leading to a decay in the applied heat flux. As the source cools, the driving temperature difference diminishes, and the measured PMD phase in the region of interest correspondingly decreases.

6. Conclusion

This work demonstrates transmission-mode phase measuring deflectometry (PMD) as an emissivity-independent technique for spatiotemporal heat-flow mapping and subsurface thermal-anomaly detection in opaque, conductive components. A controlled thermal stimulus is applied to the specimen, and the resulting heat transfer into a transparent sensing medium generates transient refractive-index gradients that distort an imaged sinusoidal fringe field. The recovered PMD phase evolution provides a quantitative, optical proxy for the underlying temperature-gradient field, enabling conduction-based thermal inspection without relying on infrared emission or emissivity calibration at the specimen surface.

Experiments on three representative anomaly classes (i) metal–metal interfaces, (ii) localized low-conductivity inserts/interlayers, and (iii) void-type geometric discontinuities within a metal host produced clear spatiotemporal phase signatures consistent with expected heat-transport

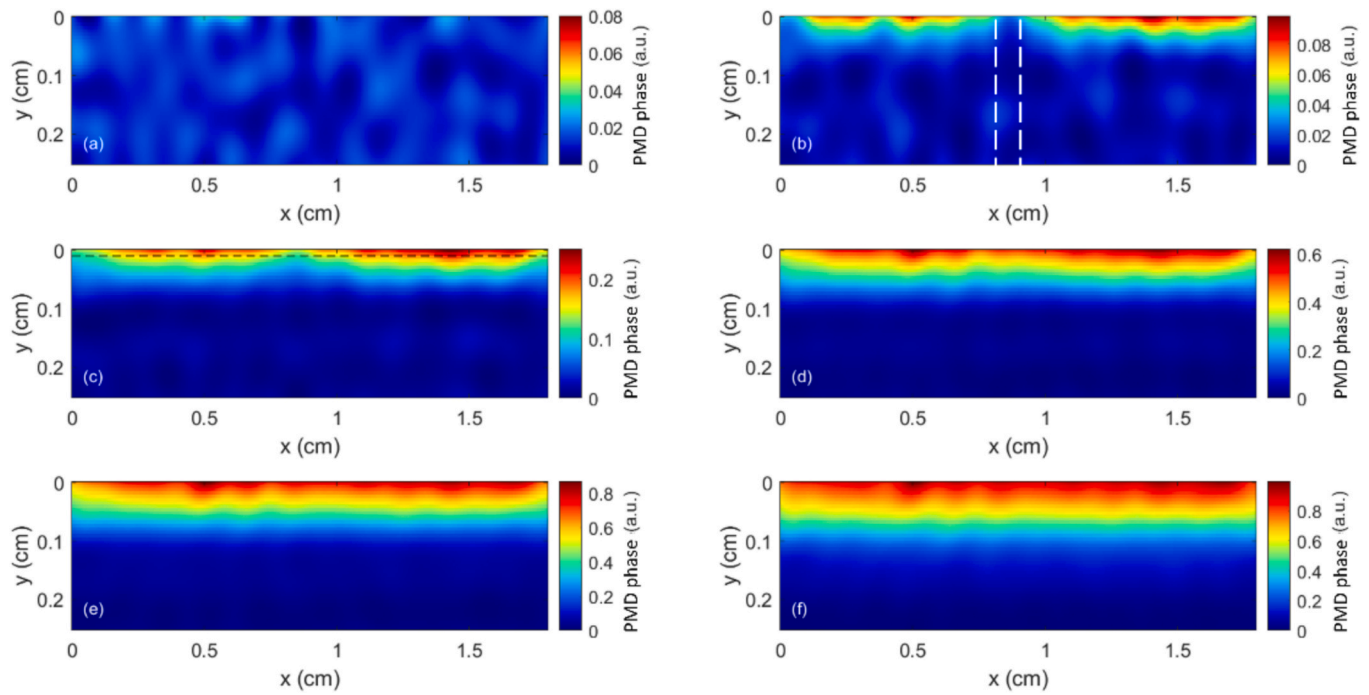

Fig. 10. Spatiotemporal evolution of the PMD phase map for Object 3 containing a cylindrical void. Times: (a) 0.33 s, (b) 0.60 s, (c) 0.93 s, (d) 1.60 s, (e) 2.27 s, (f) 3.60 s. The void perturbs local heat flow, producing a distinct PMD phase signature. (See Visualization 3.).

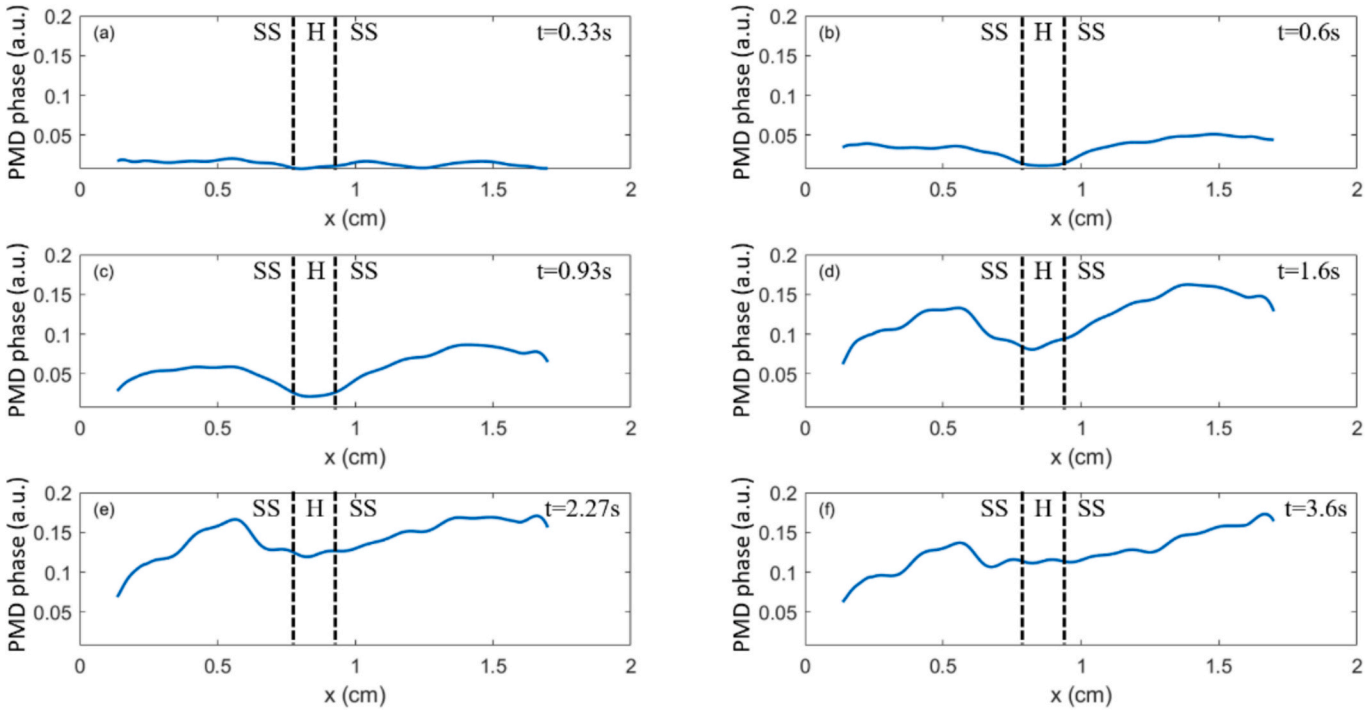

Fig. 11. PMD phase profiles along the dashed line in Fig. 10(c), showing reduced heat-flow magnitude beneath the cylindrical void.

behaviour. Across these cases, detectability is governed by the interplay between thermal-property contrast and heat-front development speed: modest contrasts (metal–metal) yield weaker but still detectable discontinuities, stronger mismatches (metal–glass–metal) produce higher contrast but can delay local heat penetration, and void-type discontinuities in an otherwise highly conductive host perturb the heat path sufficiently to become visible early in the heating transient. These representative cases provide an application-oriented baseline for rapid screening of conduction-driven anomaly signatures under controlled loading.

Quantitative validation was performed for a homogeneous aluminium reference specimen by comparing PMD-derived ROI-averaged vertical temperature gradients with a COMSOL transient heat-transfer model over the 0–3 s early-time window, which is the regime most relevant to rapid inspection and least influenced by later-stage ambient exchange and probe cooling. The agreement over this

window is strong, with a global RMSE of 0.074 K/mm between the simulated and experimentally estimated gradient time histories. Minor deviations at early times are expected because the gradients are close to zero. A modest divergence develops toward the end of the 0–3 s interval, which may arise from differences between the idealized boundary conditions in the model and the experimental thermal coupling/ambient exchange.

To characterize system-level response under variable loading, an applied thermal-load sweep was performed and the ROI-averaged phase response showed an approximately linear dependence on the applied temperature difference between the hot-water reservoir and the imaging chamber at $t = 0$. The resulting system responsivity was 0.0399 rad per unit applied ΔT_{app}. This metric is intentionally reported as an applied-load responsivity (rather than an intrinsic rad/K sensitivity to the internal ROI temperature rise), because the actual temperature change within the field of view during the early transient is small (typically $\lesssim$1 K) and not directly measurable with conventional sensors at the required spatiotemporal resolution in this proof-of-concept configuration. For physically grounded interpretation, the phase response is therefore linked to the local temperature gradient via Eq. (7) and supported by the COMSOL-derived thermal field.

The present implementation employs a hot-water reservoir as a convenient proof-of-concept thermal stimulus, selected to provide a rapid onset of uniform planar thermal loading over the specimen surface. At the same time, the hot-water source can introduce temporal variability because the driving temperature difference decays during contact. Future implementations would therefore benefit from more regulated and repeatable excitation strategies, such as PID-controlled flat resistive heaters, cartridge-heated metal contact blocks with a more uniform surface temperature, or localized optical heating, depending on specimen geometry and the desired thermal loading profile. Although the present study uses simple flat benchmark specimens, the anomaly-detection principle is not inherently restricted to planar components. If the region of interest can be coupled to a suitable transparent sensing medium and the nominal geometric response is known, anomalous regions should remain detectable through their deviation from the surrounding heat-flow signature. Extending the approach to more complex geometries and manufacturing-relevant parts will, however, require careful control of thermal coupling and excitation, accounting for heat-flow variations introduced by the sample geometry, and, where necessary, adapting the sensing medium according to specimen geometry and sensitivity requirements. For small-sized objects, fine-scale defects, or multiple defect regions, detectability is expected to depend on coupled thermal and optical factors, including defect size, depth, and spacing, thermal-property contrast, the heating-source profile, heat-transfer time through the object–interface–sensing-medium system, the thermal and thermo-optic response of the sensing medium, and the spatial resolution and phase sensitivity of the PMD system. Smaller or multiple defects may be detectable if they produce distinguishable perturbations in the measured heat-flow signature relative to the surrounding response. However, when defects are very close together, very small, or located deeper within the sample, their thermal responses can overlap or become less distinct. In such cases, improved excitation control, appropriate choice of sensing medium, and more careful analysis methods will be needed. Systematic studies using larger datasets will therefore be needed to establish detection limits for smaller and multiple anomalies and support automated defect categorization. Future work will focus on refined calibration and uncertainty quantification, improved modelling of the coupled conduction-refraction process, and automated interpretation of phase signatures to support robust deployment in inspection workflows.

Overall, the results establish transmission-mode PMD as a promising spatiotemporal, conduction-based, emissivity-independent optical inspection method for rapid thermal-gradient mapping and anomaly indication in manufactured metal components.

CRediT authorship contribution statement

Ragni Trivedi: Writing – original draft, Visualization, Validation, Methodology, Investigation, Formal analysis, Conceptualization. **Shivam Sharma:** Visualization, Validation, Software, Methodology, Investigation, Conceptualization. **Vismay Trivedi:** Writing – review & editing, Writing – original draft, Visualization, Validation, Software, Project administration, Methodology, Investigation, Formal analysis, Conceptualization. **Rahul Sharma:** Investigation, Formal analysis. **Roger M. Groves:** Writing – review & editing, Validation, Conceptualization. **Gyanendra Sheoran:** Writing – review & editing, Validation, Conceptualization. **Arun Anand:** Writing – review & editing, Validation, Supervision, Resources, Methodology, Funding acquisition, Conceptualization.

Funding

SERB (EMR/2017/002724), DAE-BRNS (2013/34/11/BRNS/504), DST-FIST, and DST-PURSE.

Declaration of competing interest

The authors declare that they have no known competing financial interests or personal relationships that could have appeared to influence the work reported in this paper.

Acknowledgement

Shivam Sharma would like to thank UGC for JRF.

Appendix A. Supplementary data

Supplementary File S1 contains details of the Fourier-transform-based phase retrieval algorithm used to generate the PMD phase maps, together with preliminary transient heat-flow simulations of the three test objects. These simulations were used to identify the time window in which the thermal anomalies are most discernible and to guide the thermal loading conditions. Videos V1–V3 show the real-time spatiotemporal evolution of the PMD phase maps for Objects 1–3, respectively, in the imaging medium immediately beneath the thermally loaded test objects. The videos illustrate the transient phase response associated with heat-flow perturbations caused by the material interface, glass insert, and internal void-type discontinuity, respectively. Supplementary data to this article can be found online at https://doi.org/10.1016/j.optlastec.2026.115664.

Data availability

Data will be made available on request.

References

[1] C. Meola, G.M. Carlomagno, Recent advances in the use of infrared thermography, Meas. Sci. Technol. 15 (9) (2004).
[2] J. Aderhold, P. Meinlschmidt, F. Schlüter, Heat flow thermography for non-destructive testing of composites and natural materials - an application-oriented overview, Tech. Mess. 87 (6) (2020).
[3] D.S.M. Serrati, M.A. Machado, J.P. Oliveira, T.G. Santos, Non-destructive testing inspection for metal components produced using wire and arc additive manufacturing, Metals (basel) 13 (4) (2023).
[4] J. Rao, S. Leong Sing, P. Liu, J. Wang, H. Sohn, Non-destructive testing of metal-based additively manufactured parts and processes: a review, Virtual Phys. Prototyp. 18 (1) (2023).
[5] D. Höfflin, C. Sauer, A. Schiffler, A. Versch, J. Hartmann, Active thermography for in-situ defect detection in laser powder bed fusion of metal, J. Manuf. Process. 131 (2024).
[6] H. Ermert, F.H. Dacol, R.L. Melcher, T. Baumann, Noncontact thermal-wave imaging of subsurface structure with infrared detection, Appl. Phys. Lett. 44 (12) (1984).

[7] V. Trivedi, M. Joglekar, S. Mahajan, N. Patel, V. Chhaniwal, B. Javidi, A. Anand, Digital holographic imaging of refractive index distributions for defect detection, Opt. Laser Technol. 111 (July 2018) (2019) 439–446.

[8] S. Utadiya, V. Trivedi, G. Sheoran, A. Srivastava, D. Claus, H. Cabrera, A. Anand, Digital holographic imaging of thermal signatures and its use in inhomogeneity identification, Opt. Lasers Eng. 160 (2023) 107227.

[9] S. Utadiya, V. Trivedi, V. Singh, G. Sheoran, H. Cabrera, A. Srivastava, B. Javidi, A. Anand, Digital holographic characterization of multilayered structures by thermal scanning, Appl. Opt. 64 (7) (2025) B134–B142.

[10] A. Kylili, P.A. Fokaides, P. Christou, S.A. Kalogirou, Infrared thermography (IRT) applications for building diagnostics: a review, Appl. Energy 134 (2014).

[11] A.A. Sarawade, N.N. Charniya, Infrared Thermography and its applications: a Review. In *Proceedings of the 3rd International Conference on Communication and Electronics Systems, ICCES*, 2018 (2018)..

[12] B.B. Lahiri, S. Bagavathiappan, T. Jayakumar, J. Philip, Medical applications of infrared thermography: a review, Infrared Phys. Technol. 55 (4) (2012).

[13] C. Da Wen, I. Mudawar, Modeling the effects of surface roughness on the emissivity of aluminum alloys, Int. J. Heat Mass Transf. 49 (23–24) (2006).

[14] C. Da Wen, I. Mudawar, Emissivity characteristics of roughened aluminum alloy surfaces and assessment of multispectral radiation thermometry (MRT) emissivity models, Int. J. Heat Mass Transf. 47 (17–18) (2004).

[15] C. Da Wen, I. Mudawar, Emissivity characteristics of polished aluminum alloy surfaces and assessment of multispectral radiation thermometry (MRT) emissivity models, Int. J. Heat Mass Transf. 48 (7) (2005).

[16] M. Wieczorowski, L. Rozanski, Roughness aspects in thermal analysis of machine tools, in: In *18th IMEKO World Congress 2006: Metrology for a Sustainable Development*, 2006, p. 2.

[17] A. Hirschberg, Schlieren and Shadowgraph Techniques: Visualizing Phenomena in Transparent Media, Eur. J. Mech. B. Fluids 21 (4) (2002).

[18] J. Ramaiah, T. de Rubeis, R. Gannavarpu, D. Ambrosini, Quantitative flow visualization by hidden grid background oriented schlieren, Opt. Lasers Eng. 160 (2023).

[19] W.L. Howes, Rainbow schlieren and its applications, Appl. Opt. 23 (14) (1984).

[20] J.M. Schulz, H. Junne, L. Böhm, M. Kraume, Measuring local heat transfer by application of Rainbow Schlieren Deflectometry in case of different symmetric conditions, Exp. Therm Fluid Sci. 110 (2020).

[21] G. Tanda, F. Devia, "Application of a schlieren technique to heat transfer measurements in free-convection," Exp, Fluids 24 (4) (1998).

[22] M.J. Hargather, G.S. Settles, A comparison of three quantitative schlieren techniques, Opt. Lasers Eng. 50 (1) (2012).

[23] P. Hariharan, *Basics of Holography*, Cambridge University Press, 2002.

[24] P.A. Walsh, M.R.D. Davies, Factors affecting temperature measurement using phase measurement interferometry in small scale devices, Exp. Therm Fluid Sci. 30 (8) (2006).

[25] M. Joglekar, V. Trivedi, V. Chhaniwal, D. Claus, B. Javidi, A. Anand, LED based large field of view off-axis quantitative phase contrast microscopy by hologram multiplexing, Opt. Express 30 (16) (2022) 29234.

[26] D. Malacara, *Optical Shop Testing*, Wiley, 2007.

[27] M. Joglekar, V. Trivedi, R. Bhatt, V. Chhaniwal, S. Dubey, D. Claus, G. Pedrini, R. Leitgeb, B. Javidi, A. Anand, Compact, low cost, large field-of-view self-referencing digital holographic interference microscope, Optik (stuttg). 245 (May) (2021) 167615.

[28] S. Utadiya, V. Trivedi, K. Bhanderi, M. Joglekar, C. Limberkar, K. Patel, G. Sheoran, H. Cabrera, B. Javidi, A. Anand, Thickness and surface profiling of optically transparent and reflecting samples using lens-less self-referencing digital holographic microscopy, Appl. Surf. Sci. Adv. 18 (2023) 100484.

[29] G.S. Settles, M.J. Hargather, A review of recent developments in schlieren and shadowgraph techniques, Meas. Sci. Technol. 28 (4) (2017).

[30] S.B. Dalziel, G.O. Hughes, B.R. Sutherland, Whole-field density measurements by "synthetic schlieren,, Exp. Fluids 28 (4) (2000) 322–335.

[31] M.J. Hargather, G.S. Settles, "Natural-background-oriented schlieren imaging," Exp, Fluids 48 (1) (2010).

[32] S. Cai, J. Liang, Q. Gao, C. Xu, R. Wei, Particle image Velocimetry based on a Deep Learning Motion Estimator, IEEE Trans. Instrum. Meas. 69 (6) (2020).

[33] C. Lagemann, K. Lagemann, S. Mukherjee, and W. Schröder, "Deep recurrent optical flow learning for particle image velocimetry data," Nat. Mach. Intell. **3**(7), (2021).

[34] V. Trivedi, M. Joglekar, S. Mahajan, V. Chhaniwal, B. Javidi, A. Anand, Portable device based on beam deflection for refractive index mapping and diffusion coefficient measurement, Opt. Eng. 58 (01) (2019) 1.

[35] F. Ciampa, P. Mahmoodi, F. Pinto, M. Meo, Recent advances in active infrared thermography for non-destructive testing of aerospace components, Sensors (switzerland) 18 (2) (2018).

[36] R. Usamentiaga, P. Venegas, J. Guerediaga, L. Vega, J. Molleda, F.G. Bulnes, Infrared thermography for temperature measurement and non-destructive testing, Sensors (switzerland) 14 (7) (2014).

[37] P.J. Tallafuss, A. Rosochowski, S. Campbell, A feasibility study on different NDT techniques used for testing bond quality in cold roll bonded Al-Sn alloy/steel bimetal strips, Manuf. Rev. (les Ulis). 4 (2017).

[38] L. Attar, M. Ech Cherif El Kettani, D. Leduc, M.V. Predoi, J. Galy, Detection of kissing bond type defects and evaluation of the bonding quality in metal/adhesive/composite structures by a wavenumber-frequency insensitive SH mode, NDT and E Int. 137 (2023).

[39] S. Karolewski, S. Borowski, K. Karolewska, Methods for diagnosing defects in glued joints – a methods review, MATEC Web Conf. 351 (2021).

[40] X. Zhang, T. Fang, J. Saniie, S. Bakhtiari, A. Heifetz, Unsupervised learning-enabled pulsed infrared thermographic microscopy of subsurface defects in stainless steel, Sci. Rep. 14 (1) (2024).

[41] V. Trivedi, M. Joglekar, S. Utadiya, N. Chhiller, S. Sharma, G. Sheoran, and A. Anand, "Shape measurement of phase objects using fringe projection technique," in *Optical Measurement Systems for Industrial Inspection XIII*, P. Lehmann, W. Osten, and A. Albertazzi Gonçalves, eds. (SPIE, 2023), p. 104.

[42] V. Chhaniwal, S. Mahajan, V. Trivedi, A. Anand, Diffusivity measurement using compact low cost field portable device based on light deflection, in: In *Optical Measurement Systems for Industrial Inspection IX*, 2015, p. 9525.

[43] S. Sharma, V. Trivedi, S. Mahajan, G. Sheoran, B. Javidi, A. Anand, Phase measuring deflectometry based microscopy for shape visualization and thickness quantification, Opt. Laser Technol. 192 (2025) 113524.

[44] S. Sharma, V. Trivedi, S. Utadiya, G. Sheoran, A. Anand, Refractometer based on phase measuring deflectometry using smartphone and machine learning assisted analysis, Phys. Scr. 100 (10) (2025) 105540.

[45] R. Trivedi, S. Sharma, V. Trivedi, R. Sharma, R. M. Groves, G. Sheoran, and A. Anand, "Heat flow visualization and thermal anomaly detection using phase measuring deflectometry," in *Optical Measurement Systems for Industrial Inspection XIV*, P. Lehmann, W. Osten, and A. Albertazzi Gonçalves, eds. (SPIE, 2025), p. 101.

[46] M. Born, E. Wolf, A.B. Bhatia, P.C. Clemmow, D. Gabor, A.R. Stokes, A.M. Taylor, P.A. Wayman, W.L. Wilcock, *Principles of Optics*, Cambridge University Press, 1999.

[47] J.H. Massig, Measurement of phase objects by simple means, Appl. Opt. 38 (19) (1999).

[48] H. Canabal, Automatic wavefront measurement technique using a computer display and a charge-coupled device camera, Opt. Eng. 41 (4) (2002).

[49] L. Huang, M. Idir, C. Zuo, A. Asundi, Review of phase measuring deflectometry, Opt. Lasers Eng. 107 (2018) 247–257.

[50] S.S. Gorthi, P. Rastogi, Fringe projection techniques: Whither we are? Opt. Lasers Eng. 48 (2) (2010) 133–140.

[51] J.L. Flores, B. Bravo-Medina, J.A. Ferrari, One-frame two-dimensional deflectometry for phase retrieval by addition of orthogonal fringe patterns, Appl. Opt. 52 (26) (2013) 6537.

[52] S. Boothaisong, S. Rittidech, T. Chompookham, M. Thongmoon, Y. Ding, Y. Li, Three-dimensional transient mathematical model to predict the heat transfer rate of a heat pipe, Adv. Mech. Eng. 7 (2) (2015).

[53] *CRC Handbook of Chemistry and Physics* (2016).